Acta metall. mater. Vol. 40, Suppl., pp. S149–S159, 1992
Printed in Great Britain. All rights reserved

0956-7151/92 $5.00 + 0.00
Copyright © 1992 Pergamon Press Ltd

ATOMIC RESOLUTION *Z*-CONTRAST IMAGING OF INTERFACES

S. J. PENNYCOOK and D. E. JESSON

Solid State Division, Oak Ridge National Laboratory, Oak Ridge, TN 37831-6030, U.S.A.

Abstract—*Z*-contrast imaging of crystals at a major zone axis is accurately described as a convolution of the scanning probe intensity profile with an object function sharply peaked at each atomic column. The object function contains the high-angle scattering cross sections and all dynamical diffraction effects, which manifest simply as a channeling effect for each individual atomic column. The channeling effect can be described entirely using highly localized *s*-type Bloch states. A tight binding formulation shows clearly that neighboring columns can be considered independently, in which case no proximity effects occur at interfaces, and it is possible to assemble object functions for interfaces, superlattices or complex unit cells from appropriate isolated string strengths which may be calculated using simpler model unit cells. Channeling effects are always less sensitive to column composition than the high-angle cross sections. Therefore, dynamical corrections to an image are always second order, and a first order intuitive interpretation can be obtained directly from the image, with no *a priori* assumptions on likely interfacial arrangements. These ideas will be illustrated for superlattices of Si_mGe_n and $(YBa_2Cu_3O_{7-x})_m(PrBa_2Cu_3O_{7-x})_n$.

Résumé—L'imagerie en contraste *Z* de cristaux suivant un axe de zone important est décrite d'une manière précise par une convolution du profil d'intensité de la sonde de balayage avec une fonction d'objet présentant un pic étroit sur chaque colonne atomique. La fonction d'objet contient les sections efficaces de diffusion aux grands angles et tous les effets de diffraction dynamiques qui se manifestent simplement par un effet de canalisation pour chaque colonne atomique individuelle. L'effet de canalisation peut être entièrement décrit en utilisant des états de Bloch de type *s* très localisés. Une formulation par liaisons fortes montre clairement que les colonnes voisines peuvent être considérées indépendamment: dans ce cas aucun effet de proximité ne se produit aux interfaces et il est possible d'assembler des fonctions d'objet pour des interfaces, des surstructures ou des mailles élémentaires complexes à partir d'intensités de chapelets appropriées isolés qui peuvent être calculés avec un modèle plus simple de maille élémentaire. Les effets de canalisation sont toujours moins sensibles à la composition des colonnes que les sections efficaces aux angles élevés. Donc, les corrections dynamiques pour une image sont toujours du second ordre, et une interprétation intuitive du premier ordre peut être obtenue directement à partir de l'image, sans aucune hypothèse *a priori* sur les arrangements interfaciaux probables. Ces idées sont développées pour les surstructures de Si_mGe_n et de $(YBa_2Cu_3O_{7-x})_m(PrBa_2Cu_3O_{7-x})_n$.

Zusammenfassung—Die Abbildung von Kristallen in Richtung einer Haupt-Zonenachse im *Z*-Kontrast wird genau beschrieben als eine Konvolution des Intensitätsprofiles der Elektronensonde mit einer Objektfunktion, die an jeder atomaren Säule ein scharfes Maximum aufweist. Diese Objektfunktion enthält die Großwinkel-Streuquerschnitte und alle dynamischen Beugungseffekte, welches sich einfach als Gitterführungseffekt bei jeder einzelnen atomaren Säule darstellt. Der Gitterführungseffekt kann mit hochlokalisierten *s*-artigen Blochzuständen vollständig beschrieben werden. Eine Tight-binding-Formulierung zeigt klar, baß benachbarte Säulen als unabhängig angesehen werden können; an den Grenzflächen treten also keine Nahwirkungseffekte auf, so daß sich Objektfunktionen für Grenzflächen, Übergitter oder komplexe Einheitszellen zusammensetzen lassen aus den entsprechenden Einzellösungen, die ihrerseits anhand von einfacheren Modellen der Einheitszellen berechnet werden können. Gitterführungseffekte sind immer weniger empfindlich gegenüber dem Ort der Atomsäule als die Großwinkel-Streuquerschnitte. Daher sind dynamische Korrekturen eines Bildes immer zweiter Ordnung; eine intuitive Interpretation erster Ordnung kann direkt von dem Bild erhalten werden, d.h. ohne irgendeine *a-priori*-Annahme einer möglichen Anordnung an der Grenzfläche. Diese Vorstellungen werden anhand von Übergittern von Si_mGe_n und $(YBa_2Cu_3O_{7-x})_m(PrBa_2Cu_3O_{7-x})_n$ erläutert.

1. INTRODUCTION

In a high-resolution scanning transmission electron microscope (STEM), a coherent electron probe can be formed with a full-width-half maximum (FWHM) intensity profile less than the projected column separations of many low-order crystal zone axes. By detecting the high-angle scattering as the focused probe scans the surface of a thin sample, the resulting image represents a map showing the location of the projected atomic columns and their relative composition, an incoherent image with resolution and contrast determined by the incident probe intensity profile at the crystal entrance surface [1, 2].

As a result of this direct correspondence between object and image, the general form of such a *Z*-

contrast image can be predicted intuitively from the crystal projection. More importantly, the optimum imaging probe is insensitive to the sample structure so that it is often possible to reverse this process and deduce the object directly from the image. For example, in the case of an interface, its structure can often be deduced to first order simply by focusing on the atomic columns either side and observing the arrangements and intensities at the interface. The key advantage is that no *a priori* information or decisions on the likely interface structure are required. No structures are excluded, so that unexpected interfacial arrangements, ordering, new interfacial phases, or transition zones will be immediately apparent and can be later confirmed by image simulation in the usual manner.

These highly desirable characteristics all arise from the use of a high-angle annular detector which was introduced by Howie [3] in order to improve the visibility of small catalyst clusters on light crystalline or amorphous supports [4]. For high-resolution imaging, the Howie detector is responsible for both the compositional sensitivity and the incoherent characteristics which will be reviewed briefly in the next section. It is also responsible for the highly localized nature of the object function, by ensuring that only the tightly bound s-type Bloch states contribute to the image. The contribution of an atomic column to the image is therefore relatively insensitive to the nature and distribution of surrounding strings. As a result, object functions for interfaces and other more complex structures can be conveniently constructed using string strengths of isolated columns, as will be discussed in Section 3 using a tight binding formulation. Finally, in Section 4, we review some of the insights which direct imaging has revealed into the actual interface structures, and the growth mechanisms which created them, in the two superlattice systems Si_mGe_n and $(YBa_2Cu_3O_{7-x})_m(PrBa_2Cu_3O_{7-x})_n$. All images were obtained with a VG Microscopes HB501 UX operating at 100 kV with a 1.3 mm C_s objective lens pole piece.

2. INCOHERENT CHARACTERISTICS AT ATOMIC RESOLUTION

2.1. Coherent or incoherent scattering?

Certain incoherent characteristics in annular detector images were noticed many years ago, even in images formed using low-angle (coherent) scattering, specifically freedom from contrast reversals and enhanced resolution [5]. This was interpreted as rising from the detector geometry [6], though we now realize that an annular detector can only average over interference fringes effectively in the transverse plane. It cannot destroy the coherence along the beam direction [7, 8] so that the intensity of a column increases initially as n^2, where n is the number of atoms in the column, then becoming oscillatory representing the familiar kinematic shape factor.

Coherence in this direction can only be destroyed by thermal vibrations, specifically multiphonon scattering events which by involving the simultaneous creation and/or destruction of large numbers of phonons will again average over many phase relationships to give a scattered intensity proportional to n, just as if the scattering were incoherently generated by each atom in the sample. The Einstein model of independently vibrating atoms is a convenient simple model of this situation and will be valid at high angles when multiphonon processes dominate the diffuse scattering [9]. The Howie detector, therefore, breaks the coherence of the imaging process in the sample and decouples Bloch states describing the incident electron flux from the Bloch states of the outgoing electrons. Such an approach was used, for example, by Bird and Wright [10] to predict Kikuchi line profiles which repesent channeling effects on the outgoing electrons.

In our case, however, the Howie detector efficiently averages over such redistribution of the outgoing flux, and the total intensity reaching the detector can be described as a simple rate of loss from the incident wavefield $\psi(r)$

$$I^{\mathrm{HA}} = \frac{2}{\hbar v}\int |\psi(\mathbf{r})|^2 V^{\mathrm{HA}}(\mathbf{R})\,\mathrm{d}\mathbf{r} \qquad (1)$$

in a manner exactly analogous to the calculation of absorption effects in dynamical diffraction [11], or the generation of X-rays [12] or low-energy photons [13]. In the present situation $V^{\mathrm{HA}}(\mathbf{R})$ is the projected potential for scattering to the high-angle detector including the effects of thermal smearing. Explicit expressions for the high-angle potential can be obtained from the treatment of Hall and Hirsch [11] simply by restricting the range of integration to the angular range of the Howie detector [2].

Since the inner angle of the detector is very large compared to typical Bragg angles, the potential is correspondingly very sharply peaked in real space, ~0.2 Å full width half maximum (FWHM) for a 75 mrad inner detector angle. This is significantly sharper than even the most localized Bloch states, and it is often convenient, though by no means essential, to make the approximation of complete localization, replacing equation (1) by

$$I^{\mathrm{HA}} = \frac{2}{\hbar v}\sum_{\kappa}|\psi(\mathbf{r}_\kappa)|^2\int V^{\mathrm{HA}}(-\mathbf{r})\mathrm{d}\mathbf{R} = \sum_{\kappa}|\psi(\mathbf{r}_\kappa)|^2\sigma_\kappa \qquad (2)$$

which makes clear the connection to the atomic high-angle scattering cross section. In effect, the detector has been transferred to the atomic sites themselves.

We emphasize that the single phonon model of Wang and Cowley [14, 15] is entirely inappropriate for describing high-angle scattering, since it is based on the small-angle approximation of Takagi [16]. It ignores entirely the multiphonon contribution which dominates at high angles and therefore predicts a

much reduced diffuse component, as well as an unphysical doughnut-shaped scattering potential which is not peaked at the projected atom sites. More recent attempts to include such processes into the multislice formulation [17] have incorrectly summed the multiphonon contributions, and therefore preserves the unphysical form of the scattering potential.

2.2. Zone axis imaging of crystals

Consider now the case of a crystal viewed along a low-order zone axis. If the crystal is very thin, it will act as a phase object, and the probe intensity profile inside the crystal will, therefore, be identical to that of the incident probe. We can arrange for the detector to collect only diffuse scattering by making the inner detector angle sufficiently large (150 mrad for Si at room temperature, see Fig. 1), in which case the image intensity will again be given by equations (1) and (2). If the probe is sufficiently fine to resolve the atomic columns, then the resulting compositional map will show atomic resolution. Standard incoherent imaging theory can be used to describe the image as a convolution between the incident probe intensity profile $P^2(\mathbf{R})$ and an object function $O(\mathbf{R})$ sharply peaked at the projected atomic columns, giving

$$I^{\mathrm{HA}}(\mathbf{R}) = O(\mathbf{R}) * P^2(\mathbf{R}) \tag{3}$$

where

$$O(\mathbf{R}) = \sum_i \sigma_i^{\mathrm{c}}\, \delta(\mathbf{R} - \mathbf{R}_i) \tag{4}$$

is the crystal object function written for simplicity in the limit of complete localization, and $\sigma_i^{\mathrm{c}} = 1/t\ \Sigma_\kappa\, \sigma_\kappa$ is the high-angle cross section of atomic column i at position $\mathbf{R}_i$ with length t. Typically, these have not yet reached their full unscreened values corresponding to Rutherford scattering, but the Born approximation also fails severely for any but the lightest atoms so that the usual Doyle and Turner [18] scattering factors cannot be used. Various expressions for the cross sections have been discussed in Pennycook *et al.* [19] and are illustrated for the case of Bi in Si in Fig. 2. The best analytical approximation appears to be a form due to Fleischmann [20] which gives

$$\sigma \propto Z^2\left[\frac{\theta_2 - \theta_1}{\theta_1\theta_2\theta'_\alpha} + \frac{1}{\theta'^2_\alpha}\ln\frac{\theta_1}{\theta_2}\cdot\frac{(\theta_2+\theta'_\alpha)}{(\theta_1+\theta'_\alpha)}\right] \tag{5}$$

where θ_1 and θ_2 are the inner and outer detector angles and θ'_α is a modified screening angle given as

$$\theta'^2_\alpha = \mathrm{e}\theta_0^2(1.13 + 3.76\alpha^2) \tag{6}$$

where $\alpha = Z/137\beta$; $\beta = v/c$, where v is electron velocity; and $\theta_0 = 1.13Z^{1/3}/137\beta$, the Born screening angle. Note that the Born approximation cross sections predict a relative scattering power of Bi to Si almost twice as great as that observed experimentally. For species which differ less in their relative atomic number, the discrepancy is reduced. More accurate partial wave calculations have also been performed [21].

With a phase object, the high inner angle required to ensure only diffuse scattering is detected will result in a very weak signal. More efficient imaging can be achieved by reducing the inner detector angle to 30–50 mrad and detecting the coherent scattering. Incoherent characteristics will be seen in the transverse plane, provided the detector averages a sufficient number of fringes, and equation (3) can again be used to interpret the image [7, 8]. Now, however, the object function for a column becomes a coherent integration along its length, increasing initially as the square of the number of atoms, then oscillating as shown in Fig. 3, representing the usual kinematical shape factor for diffracted intensities. With awareness of the thickness behavior, this approach represents a useful extension of incoherent imaging to thin crystals and explains the characteristics observed previously in experimental and calculated images of atom clusters.

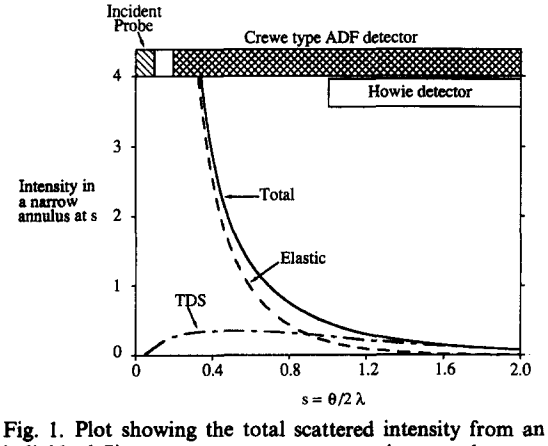

Fig. 1. Plot showing the total scattered intensity from an individual Si atom at room temperature integrated over a narrow annulus at $s = \theta/2\lambda$ and its decomposition into coherent elastic scattering and thermal diffuse scattering (TDS). Also shown are typical angular ranges for the objective aperture, the low-angle annular detector, and the Howie detector.

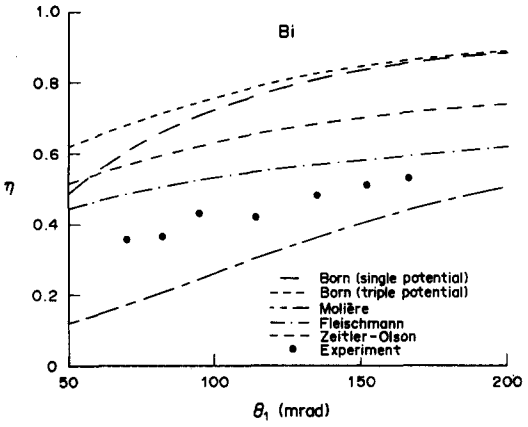

Fig. 2. Comparison of experimental and theoretical predictions for the ratio of Bi to Si cross sections, as a function of inner detector angle θ_1, expressed in terms of $\eta = (\sigma_{\mathrm{Bi}}/\sigma_{\mathrm{Si}})\cdot(Z^2_{\mathrm{Si}}/Z^2_{\mathrm{Bi}})$, ($\eta = 1$ for unscreened Rutherford scattering).

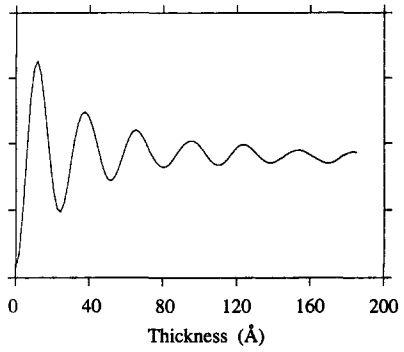

Fig. 3. Intensity of the zero layer coherent diffraction reaching a 50–150 mrad Howie detector as a function of thickness, using a probe of 10.3 mrad semiangle located over a dumbbell in Si⟨110⟩.

Note that the coherent intensity never rises above that scattered by a thin crystal, so that with increasing thickness the detected intensity will soon be dominated by the diffuse scattering. Therefore, with samples which are not too thin, the inner angle of the Howie detector can be significantly reduced from the 150 mrad implied by Fig. 1 and still collect predominantly thermal diffuse scattering. With a 75 mrad inner angle, for example, the coherent signal from a 50 Å thick Si⟨110⟩ crystal at room temperature is only 2% of the diffuse intensity, and three-dimensional incoherent imaging returns. However, the object function must now include only the diffuse component, with a cross section $\sigma_\kappa^{\mathrm{TDS}}$ given by

$$\sigma_\kappa^{\mathrm{TDS}} \propto \int_{\mathrm{detector}} f_\kappa^2(s)\left[1 - \mathrm{e}^{-2M_\kappa s^2}\right] \mathrm{d}^2\mathbf{s} \qquad (7)$$

where $f_\kappa(s)$ is the atomic scattering factor, $s = \theta/2\lambda$, θ is the scattering angle, and λ is the electron wavelength. The factor in square brackets is quite sensitive to the Debye–Waller factor M_κ, and to the scattering angle θ as apparent from Fig. 1. It can significantly alter the relative contrast of different species or sites from that expected from the ratios of the atomic scattering factors alone.

In addition, static strain fields due to distributed point defects or impurities may now give rise to bright contrast through this term [22]. The effective atomic cross section is increased by the static strain field, whereas the intensity at the sites will be decreased [see equation (2)]. The contrast can therefore change from bright to dark with increasing detector angle.

2.3. Bloch state filtering

For a sufficiently thick crystal, axially aligned, and a sufficient inner detector angle, the signal collected will be dominated by multiphonon diffuse scattering. Equations (1) or (2) can be used to calculate the image, provided that dynamical diffraction effects are included in calculating the intensity felt by each atomic site. In marked contrast to conventional high-resolution imaging, it is found experimentally that no strong interference effects are apparent in the image, which simply increases in intensity and then gradually reduces in contrast but with no obvious change in form. This remarkable behavior is again the direct result of the Howie detector. By detecting only the flux scattered close to the atomic columns, it imposes a very strong filter on the fast electron Bloch states; s-type Bloch states tightly bound to the columns will obviously be very efficient in scattering to the detector whereas p-type states which tend to peak between the strings will clearly be much less effective.

This tendency is further enhanced by the coherent angular integration over the incident probe. The tightly bound states are nondispersive and add constructively to give a strongly enhanced amplitude at the strings. Less bound states are correspondingly more dispersive and do not add in phase. This behavior explains the channeling effect observed previously by Fertig and Rose [23] and Loane *et al.* [24], in which the probe was seen to peak sharply at the atomic strings with an envelope corresponding to the incident probe profile. In our case, it means that s-states are almost entirely responsible for the Z-contrast image. This has been demonstrated for the case of Si⟨110⟩ by comparing the results of full dynamical calculations with those for s-states alone, where it was found that the s-states were responsible for practically the entire image contrast [1, 2]. It should be noted that Si⟨110⟩ provides a relatively severe test case since by summetry, p-type Bloch states are quite highly excited even on axis. In projections comprising only a single string per unit cell, the p-state contribution will be even lower.

It is this combination of the Howie detector and the coherent STEM probe which is responsible for extending the incoherent nature of Z-contrast imaging to practical sample thicknesses. With the image determined primarily by s-states, there can be no strong depth dependent interference phenomena with other Bloch states. This is true even if the low-order diffracted beams are interfering strongly to give the familiar thickness dependence of conventional phase or diffraction contrast images. In conventional imaging, the filtering is entirely reversed; the high order components of the s-states are filtered out by the objective aperture, and we no longer have a coherent angular integration of Bloch states, with the result that there is no strong enhancement of the s-state contribution relative to other less-localized states. Furthermore, only the wavefunction at the exit face is utilized, and strong depth dependent interference effects result, as discussed for the case of Si⟨110⟩ by Kambe [25]. In the Z-contrast case, however, we retain the essential features of incoherent imaging. The primary effect of dynamical diffraction is that the columnar object function contains not only the scattering cross sections, but the thickness integrated s-state intensity at the atom sites, which represents the column's channeling effect.

3. IMAGING WITH TIGHTLY BOUND STATES

To an excellent approximation, therefore, we may consider the image to be due entirely to s-type Bloch states tightly bound to individual atomic columns. In the case of only one dominant s-state (or cluster of bonding and antibonding combinations in the case of two or more identical strings per projected unit cell), the simplest treatment is to consider this state (or cluster) independently, in which the object function is given simply by

$$O(\mathbf{R}) = \sum_i \sigma_i^c \epsilon^{1s2}(0) b^{1s2}(0, \mathbf{R}_i)\left(\frac{1 - e^{-2\mu^{1s}t}}{2\mu^{1s}}\right) \quad (8)$$

where $\epsilon^{1s}(0)$ and μ^{1s} are the excitation and absorption coefficients for the Bloch state $b^{1s}(0, R)$ calculated for axial illumination, and t is the object thickness. The incident probe intensity profile is now replaced with an effective probe intensity profile

$$P_{\text{eff}}^2(\mathbf{R}) = \left|\frac{1}{\epsilon^{1s}(0)}\int_{\text{probe}} \epsilon^{1s}(\mathbf{K}) e^{i[\mathbf{K}\cdot(\mathbf{R}-\mathbf{R}_0)+\gamma(\mathbf{K})]}\, d\mathbf{K}\right|^2 \quad (9)$$

which includes the angular fall off in the excitation of the s-state cluster. $\gamma(\mathbf{K})$ is the usual transfer function phase factor for spherical aberration and defocus. Since the s-states are significantly narrower in real space than currently attainable probes, this fall off is relatively small for a typical optimum objective aperture and has little effect on the overall probe shape, so to a good approximation we can write

$$P_{\text{eff}}^2 = S^2(K_c)P^2 \quad (10)$$

where

$$P = \int_{\text{probe}} e^{i[\mathbf{K}\cdot(\mathbf{R}-\mathbf{R}_0)+\gamma(\mathbf{K})]}\, d\mathbf{K} \quad (11)$$

is the incident probe, $S(K_c)$ is a scaling factor given by

$$S(\mathbf{K}_c) = \int \epsilon^{1s}(\mathbf{K})\, d\mathbf{K}/\pi K_c^2 \epsilon^{1s}(0) \quad (12)$$

and K_c is the objective aperture cutoff. For more complex materials in which S differs for different columns, this factor can then be conveniently incorporated into the object function [2]

Treating the s-states independently results in an object function which in the absence of absorption would increase linearly with specimen thickness. It cannot reproduce the oscillatory behavior seen with the full dynamical calculation in Fig. 4 and does not reduce to the correct limit [equation (4)] in thin crystals. A better approximation is obtained by realizing that the s-states, with the largest transverse energy, will be the first to acquire a distinct phase due to propagation along the z-axis. The dynamical oscillations at small thicknesses therefore arise through interference of the 1s state cluster $\epsilon^{1s}b^{1s}$ with the sum of all other states $1 - \epsilon^{1s}b^{1s}$ as these two components propagate with different phase factors. Taking the zero of transverse energy to coincide with

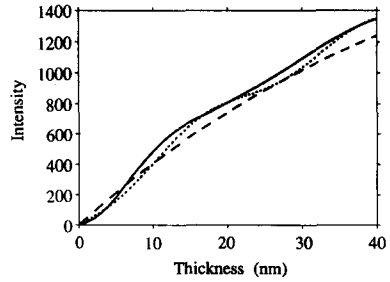

Fig. 4. Thickness integrated intensity at the atom sites in Si⟨110⟩ for an incident probe located over a dumbbell using the full dynamical calculation (solid line), the 1s state alone [equation (7), dashed line], and the 1s state channeling approximation [equation (11), dotted line].

the cluster of other states at the top of the potential wells, the wavefunction can be written as

$$\psi(\mathbf{R}, z) = P_{\text{eff}}(\mathbf{R})\epsilon^{1s}(0)b^{1s}(0, \mathbf{R})\, e^{is^{1s}z/2\chi}\, e^{-\mu^{1s}z} + [P(\mathbf{R}) - P_{\text{eff}}(\mathbf{R})\epsilon^{1s}(0)b^{1s}(0, \mathbf{R})]\, e^{-\mu_0 z} \quad (13)$$

where μ_0 represents the mean absorption coefficient. Integrating the intensity along the columns as before leads to the object function

$$\begin{aligned} O(\mathbf{R}) = \sum_i \sigma_i^c \Bigg\{ & S^2(K_c)\epsilon^{1s2}(0)b^{1s2}(0, \mathbf{R}_i)\left(\frac{1 - e^{-2\mu^{1s}t}}{2\mu^{1s}}\right) \\ & + [1 - S(K_c)\epsilon^{1s}(0)b^{1s}(0, \mathbf{R}_i)]^2\left(\frac{1 - e^{-2\mu_0 t}}{2\mu_0}\right) \\ & + \frac{2S(K_c)\epsilon^{1s}(0)b^{1s}(0, \mathbf{R}_i)}{(\mu^{1s} + \mu_0)^2 + s^2/4\chi^2} \\ & \times [1 - S(K_c)\epsilon^{1s}(0)b^{1s}(0, \mathbf{R}_i)] \\ & \times \Bigg[e^{-(\mu^{1s}+\mu_0)t}\left(\frac{s^{1s}}{2\chi}\sin\frac{s^{1s}t}{2\chi} \right. \\ & \left. - (\mu^{1s} + \mu_0)\cos\frac{s^{1s}t}{2\chi}\right) + \mu^{1s} + \mu_0 \Bigg] \Bigg\}. \end{aligned} \quad (14)$$

This approach is similar to the channeling approximation of Van Dyck [26] and gives much better agreement with the full dynamical result in the thin crystal regime. In the absence of absorption, equation (14) simplifies to

$$\begin{aligned} O(\mathbf{R}) = \sum_i \sigma_i^c \Bigg\{ & S^2(K_c)\epsilon^{1s2}(0)b^{1s2}(0, \mathbf{R}_i)t \\ & + [1 - S(K_c)\epsilon^{1s}(0)b^{1s}(0, \mathbf{R}_i)]^2 t \\ & + 2S(K_c)\epsilon^{1s}(0)b^{1s}(0, \mathbf{R}_i)[1 - S(K_c) \\ & \times \epsilon^{1s}(0)b^{1s}(0, \mathbf{R}_i)]\frac{2\chi}{s^{1s}}\sin\frac{s^{1s}t}{2\chi} \Bigg\}. \end{aligned} \quad (15)$$

Such a treatment can be extended fairly readily to handle situations where more than one bound s-state is important, as occurs for heavier strings.

States of this nature are well described by the real space tight binding method of Kambe *et al.* [27], and this formulation provides substantial further insight into the nature of the object function. Bloch states are

now constructed from states ϕ^j of the isolated strings. In the simplest case of a lattice with only one string per unit cell and only one bound s-state, the Bloch state τ^{1s} is given simply as

$$\tau^{1s}(\mathbf{K}, \mathbf{R}) = \phi^{1s}(\mathbf{R} - \mathbf{R}_i) + \sum_{\mathbf{l} \neq 0} \phi^{1s}(\mathbf{R} - \mathbf{R}_i - l)\, e^{i\mathbf{K}\cdot\mathbf{l}} \tag{16}$$

where $\mathbf{l}$ is a lattice vector of the primitive projected cell. Clearly, if ϕ^j is highly localized compared to the string separation, the overlap terms will be negligible, and the Bloch state becomes nondispersive. Tight binding theory, therefore, justifies our removal of the s-type states from the angular integration and shows in this limiting case that the Bloch states $\tau^j(0, \mathbf{R}) = b^j(0, \mathbf{R})$ are identical with the isolated string states $\phi^j(\mathbf{R})$. Note too that if the neighboring strings are different types, their bound states are likely to be at different transverse energies reducing the likelihood of overlapping states.

Furthermore, a good estimate of the object function requires accuracy only in the intensity of the s-states, not their eigenvalues, since the eigenvalues only affect the periodicity of the small dynamical oscillations in the thickness dependence. We are, therefore, relatively insensitive to small overlaps with the tails of the potentials from neighboring strings. If the tail of one state is relatively uniform over the s-state at a neighboring site, the effect will be similar to a change in the mean inner potential and will only affect the eigenvalue. In phase contrast imaging, such small changes in the eigenvalue are directly converted to changes in the image intensity [25], so that strong proximity effects would be likely even if only s-states were involved in the imaging. Of course, less localized states are also involved in phase contrast imaging, and these are far more sensitive to overlaps with neighboring strings, with the result that proximity effects are inherent and images from interfaces must be calculated explicitly using a complete structure model for the interface. This is the key reason why it is difficult to interpret a phase contrast image directly in terms of likely column positions and scattering powers [26].

If the spacing between strings becomes comparable to the width of the bound states, then substantial overlap may occur. This happens in the case of the Si or Ge dumbbells which occur in the ⟨110⟩ projection. It can also occur for non-identical strings between states of different principle quantum numbers, for example a $3s$ state on a heavy string may hybridize with a $2s$ state on a lighter string. Such cases could, of course, be handled within tight binding theory by evaluating the overlap integrals, but the ease with which many beam axial Bloch state calculations can handle the situation means that there is little incentive to use the tight binding approach for numerical calculation, at least in the crystals studied so far. In the many beam approaches, the appropriate molecular orbital combinations naturally appear and can be readily identified as such [28]. The two approaches could, of course, be combined using the many beam method to determine molecular orbital basis states and treating the weaker overlap from cell to cell through tight binding.

Figure 5 illustrates some highly excited Bloch states for a Si_2Ge_2 superlattice. Two highly localized states are shown, corresponding to bonding s-type molecular orbitals located over the Si and Ge dumbbells respectively, and also two less localized states, one centred primarily over the Ge dumbbell, the other representing a hybridization of a Ge $2s$ state with the $2p$ states of the weaker Si strings. Obviously, these delocalized states, important in phase contrast imaging, are substantially modified from the corresponding states in the perfect crystals, whereas the two s-state molecular orbitals responsible for the Z-contrast image differ by less than 1% of their intensities in the respective single crystals. In fact, even for substantial overlap seen within the dumbbells, the intensities at the sites differ by only 10% from the values calculated for individual isolated columns [29].

The fact that Z-contrast images of perfect crystals can be described in terms of the s-states of isolated strings, or molecular orbital combinations of s-states, is the key reason for the interpretability of the images. It explains the widespread lack of proximity effects at interfaces and allows us to build object funcions for interfaces, superlattices, or complex unit cell materials from appropriate isolated string strengths.

4. DIRECT IMAGING AT ATOMIC RESOLUTION

We have seen how the wide angular range of the illuminating STEM probe (which necessitates a coherent angular integration of Bloch states), together with the high-angle detector (which senses only the integrated intensity at the atom sites), act as a very efficient Bloch state filter to reduce interference effects to second order, both in regard to the thickness dependence of the image and in regard to the interaction of neighboring columns. With dynamical effects reduced to second order, the dominant factor governing the image contrast becomes the high-angle scattering cross section of the column. This is the reason why Z-contrast images can be interpreted intuitively to first order, and unanticipated interfacial atomic arrangements will be immediately apparent from the image.

Consider, for example, an alloy $Si_{1-x}Ge_x$ viewed along the ⟨110⟩ projection. There is very little variation in the bonding s-state molecular orbital intensity with alloy composition x, as shown in Fig. 6. This is because with increasing string strength, although the state becomes more sharply peaked at the atomic sites, its excitation becomes correspondingly reduced. As a function of thickness, the ratio of Ge to Si s-state intensities show a general decrease, reflecting the higher absorption of the Ge column, as shown in Fig. 7. The full dynamical calculation indicates a

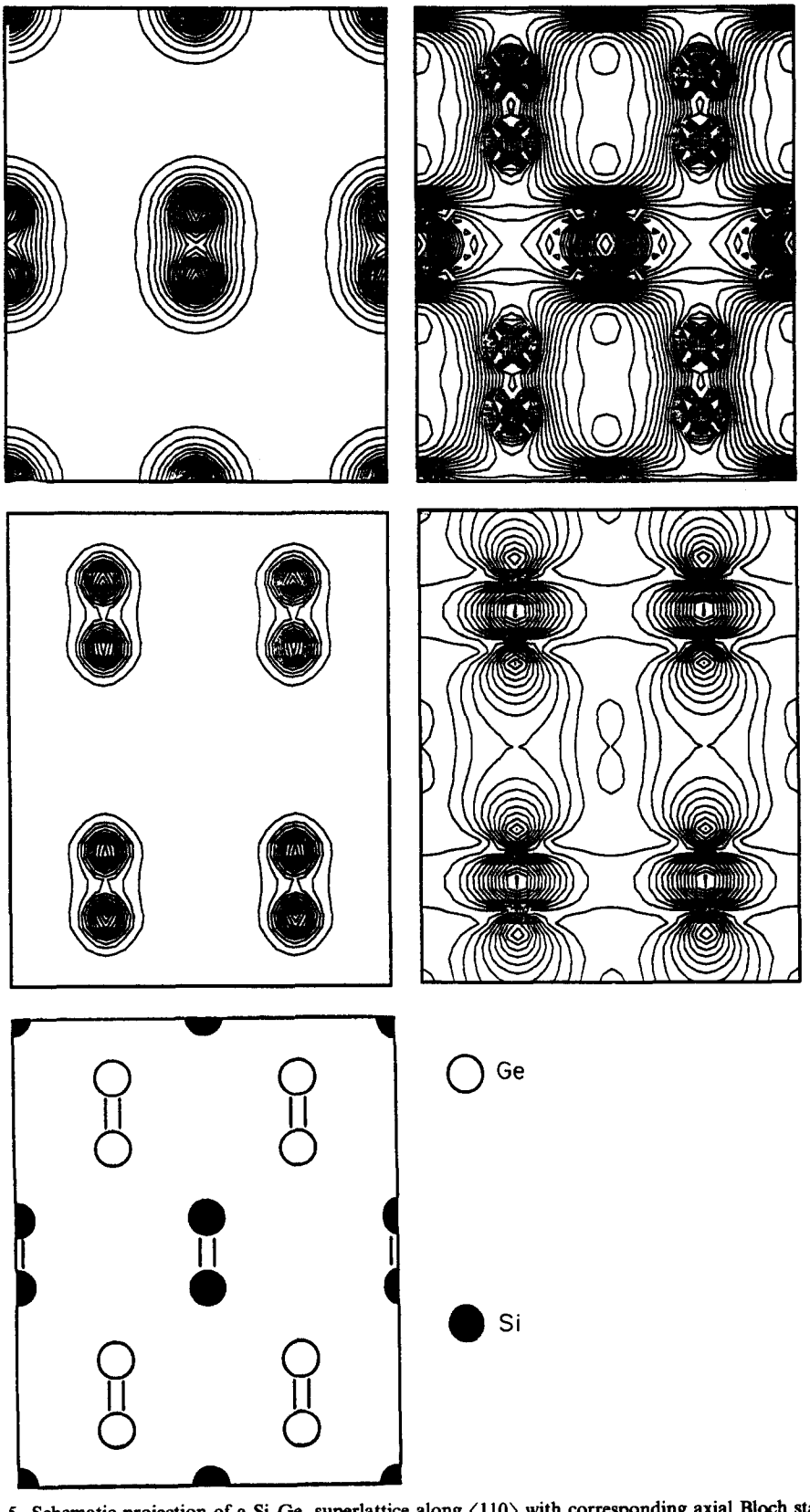

Fig. 5. Schematic projection of a Si_2Ge_2 superlattice along ⟨110⟩ with corresponding axial Bloch states for a 100 kV electron, showing bonding *s* molecular orbital states around individual Si and Ge dumbbells (upper states) and two less localized states as described in the text (lower states).

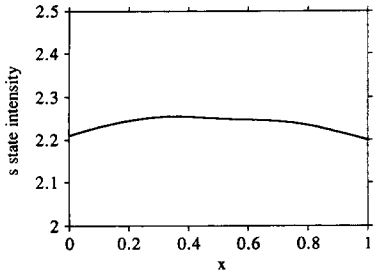

Fig. 6. Variation in s-state intensity $(\epsilon^{1s}b^{1s})^2$ with alloy composition x in $\langle 110 \rangle$ $Si_{1-x}Ge_x$.

dynamical enhancement at a thickness of 3–6 nm of approximately 20% towards Ge. A reasonable approximation to this behavior is obtained with the s-state channeling approximation, equation (14). However, it is quite clear that this factor is second order compared to the cross section ratio of 3.7. This ensures that throughout the thickness range, an increase in Ge concentration will always result in an increase in image intensity, providing intuitive interpretability of relative column compositions to first order. More accurate quantification can then be made through image simulations incorporating dynamical corrections to the object function.

In the case of the $(YBa_2Cu_3O_{7-x})_m$ $(PrBa_2Cu_3O_{7-x})_n$ superlattices, viewed normal to the c-axis, we need to discriminate between Y and Pr columns. In these calculations, we have made use of the insights provided by the tight binding analysis and the channeling approximation which demonstrated how the entire image contrast is due to s-states and their interactions. Details of the weakly bound states are unimportant so that we can model the behavior of individual Y, Ba and Pr strings in the superconductor using tetragonal model unit cells having an appropriate c lattice parameter (corresponding to a or b of the superconductor) and an adjustable a lattice parameter. Convergence with full 241 beam calculations for the complete unit cells was achieved with a 3 Å spacing of strings using only 45 beams. As with $Si_{1-x}Ge_x$, we find the variation in 1s state intensity for a column of $Y_{1-x}Pr_x$ is relatively minor (Fig. 8), even compared to the reduced cross section ratio of 1.9.

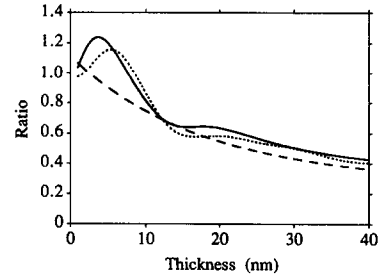

Fig. 7. Ratio of integrated s-state intensity in Ge to Si as a function of thickness, using the full dynamical calculation (solid line), the 1s state alone (dashed line), and the 1s state channeling approximation (dotted line).

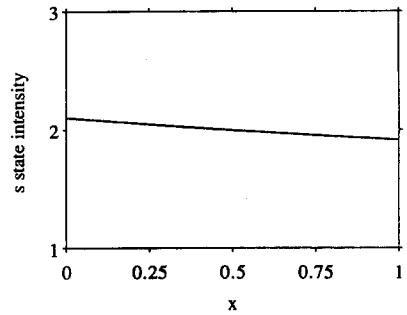

Fig. 8. Variation in 1s state intensity as a function of composition for a column of $Y_{1-x}Pr_x$.

Now, however, the effects of absorption on the heavy Pr string are much more severe. Absorption was included by the method of Bird and King [30] using Debye–Waller factors of 0.56 for Y [31] and the same for Pr in the absence of more accurate information. The thickness dependence was calculated using the full dynamical calculation to include all interactions of higher order s-states. As seen in Fig. 9, the integrated intensity along the Y string rapidly exceeds that for the strongly absorbed Pr string and is predicted, in fact, to exceed the cross section ratio. This would imply a reversal in contrast which has not been seen experimentally, though the contrast does decrease rapidly with thickness as shown in Fig. 10(a). Most likely, the absorption effect is somewhat over-estimated as a result either of uncertainties in the Debye–Waller factor or perhaps in the validity of an Einstein model in calculating the s-state absorption. Careful matching of theory to experiment may well provide a method to develop more accurate descriptions of electron absorption affects. There is also a small contribution to the image intensity from the absorbed electrons themselves, as they traverse the remainder of the sample, though since they see only the average composition, it seems likely that this contribution will be minor. In practice, however, the best compositional contrast is clearly obtained from the thinnest regions of the sample and again is directly interpretable within the limit set by image statistics.

So far, we have been concerned entirely with the nature of the object function. It is, of course, of paramount importance that the highly local nature of

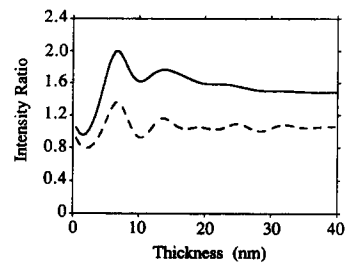

Fig. 9. Ratio of integrated intensities in Y to Pr as a function of thickness using a full dynamical calculation including absorption (solid line) and with no absorption (dashed line).

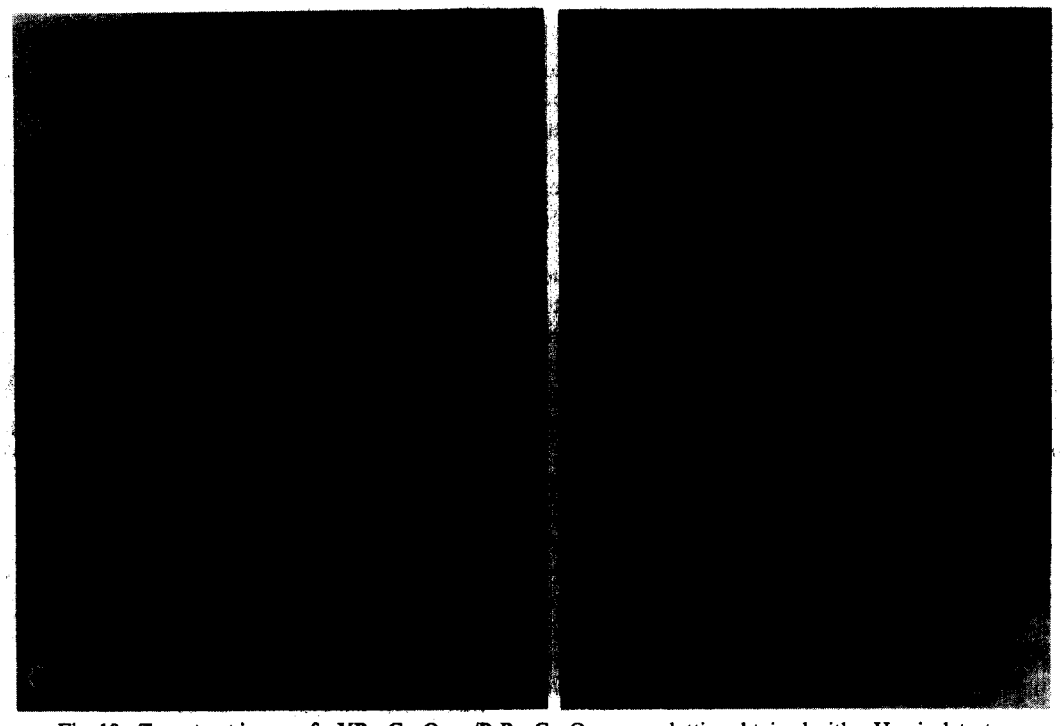

Fig. 10. Z-contrast image of a $YBa_2Cu_3O_{7-x}/PrBa_2Cu_3O_{7-x}$ superlattice obtained with a Howie detector covering 75–150 mrad; (a) shows wavy compositional modulations and decreasing contrast with thickness, (b) shows a Y plane changing abruptly to a Pr plane at an interfacial step, whereas the Ba planes continue unaffected.

the object function be preserved as far as possible after convolution with the scanning probe. For direct imaging, we obviously need a highly localized probe. A nonlocal probe can arise in two ways; either with a small objective aperture and small defocus value giving a broad diffraction limited probe with loss of both resolution and contrast, or at large objective apertures and large defocus values, when large subsidiary maxima can surround the central peak. If such subsidiary maxima coincide with neighboring columns, then severe compositional smearing will occur, and it becomes very difficult to visualize the effect of the convolution with such complicated probe shape. The image resolution can actually improve with a probe of this nature due to the narrowing of the central peak [32, 33]. Note that contrast transfer functions analyze only the spatial frequency content of the probe and so do not address the issue of localization. Direct imaging needs a compact, simple probe shape such as the modified Airy disc obtained under Scherzer optimum incoherent conditions (aperture semiangle $(4\lambda/C_s)^{1/4}$ and defocus—$(C_s\lambda)^{1/2}$, see Scherzer [34], also Ref. [2]).

5. MATERIALS INSIGHTS FROM DIRECT IMAGING

Under optimum conditions, direct imaging of interface structure and composition can be achieved without the need for any preconceived ideas concerning likely model structures. Unanticipated structures will be immediately apparent and can give dramatic insight into interfacial properties and the growth mechanisms by which such structures arose.

In semiconductor materials grown by molecular beam epitaxy, we have found several examples in which the actual interface structures differed substantially from the model interface structures considered previously, as a result of the crucial role of kinetic factors in low temperature growth [35, 36]. Figure 11

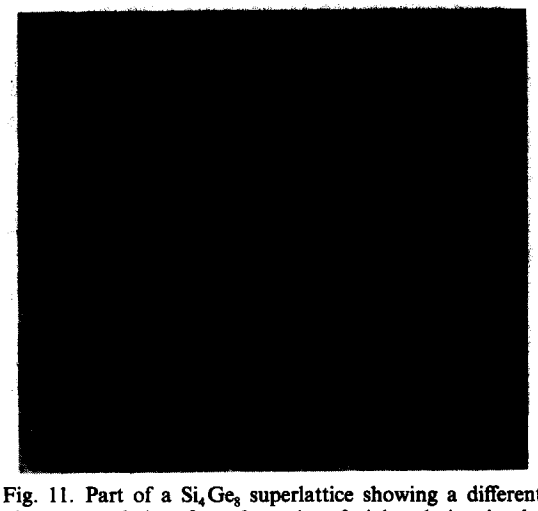

Fig. 11. Part of a Si_4Ge_8 superlattice showing a different phase at each interface, $2 \times n$ interfacial ordering in the upper Si layer, {111} planar ordering in the central Si layer, and cross-like structures in the lower layer. Sample thickness is decreasing towards the top of the image.

shows part of a Si_4Ge_4 ultrathin superlattice revealing an unexpected complexity in interfacial structure, in fact a different atomic rearrangement at each interface. Obviously, such an image is extremely important in attempting to understand the optical properties of the material, but it also directly reflects the atomistic processes which occurred during growth. A very plausible Ge atom pump model involving interchange of a Ge adatom with an underlying Si atom at one of the two district step configurations which occur when a new monolayer advances over a 2×1 reconstructed surface explains the various ordered arrangements observed and the asymmetric interfacial abruptness [37]. The lateral size of ordered domains correlates well with the size of islands observed by scanning tunneling microscopy.

It is most unlikely that such a complex arrangement of different phases would ever be considered as a likely trial structure for fitting to diffraction data (and even less likely that a fit would be believed). It is also unlikely that the atom pump would be seen spontaneously in any molecular dynamics calculation of surface processes. The direct image of the interface structure provides a new depth of insight into materials behavior.

In the case of the superconducting superlattices, the images of Fig. 10 indicate perfect crystallinity but a wavy compositional modulation, which again directly reflects the nature of the growth process. The surface supersaturation during growth was low enough for sufficient surface mobility to avoid structural defects, but high enough that island growth occurred with associated roughening of the growing surface. From images of single unit cell superlattices, it was seen clearly that cell-by-cell growth was occurring, a layer one unit cell thick completing almost perfectly before the next layer nucleated [38]. From the spacing of interfacial steps, the intrinsic island size

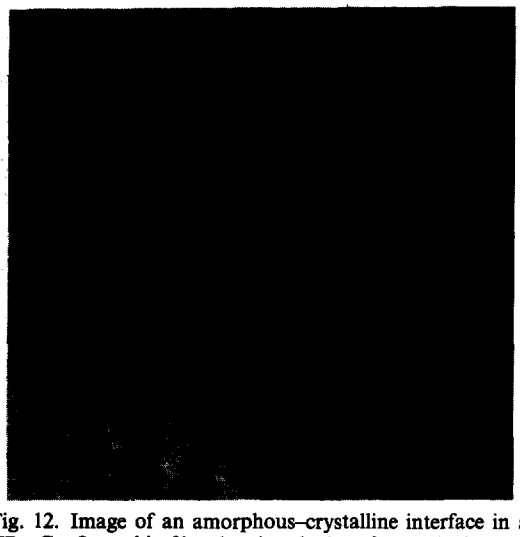

Fig. 12. Image of an amorphous–crystalline interface in a $YBa_2Cu_3O_{7-x}$ thin film showing the interface to be located predominantly at the Cu-chain plane but jumping repeatedly by a complete unit cell.

Fig. 13. The interface between a rather defective $YBa_2Cu_3O_{7-x}$ film and the $KTaO_3$ substrate showing a transition zone approximately 8 Å wide as indicated in the schematic.

could be deduced, and the preferred surface termination was seen to be Cu-chain plane (Fig. 12). With higher supersaturations, this morphology could not be maintained, and the growth proceeded with the *a–b* plane as the growing surface. Under these conditions, substantial roughness was seen on the microscopic scale in the form of pillars one or two unit cells in area extending out of the surface.

These insights into growth mechanisms result directly from the incoherent nature of the images and their compositional sensitivity which allows each interface of the superlattice to present a snapshot of the state of the growing surface at that particular time, a snapshot obtained under the true conditions of supersaturation. Even scanning tunneling microscopy has not provided this clear vision of growth since it lacks compositional sensitivity and for these materials has not demonstrated atomic resolution in the surface plane. Neither, of course, can it detect any subsurface atomic rearrangements which may occur later, though in the present case, none seem to have occurred; the observation of a sharp interface step in Fig. 10(b) represents the best direct evidence that interdiffusion is insignificant. Interdiffusion is important since it would substantially alter the superconducting properties of the superlattices. The onset of interdiffusion would be seen as a smearing at such a step, since diffusion within the *a–b* plane is substantially faster than diffusion along the *c*-axis.

Figure 13, however, shows the interface between the $YBa_2Cu_3O_{7-x}$ film and a $KTaO_3$ substrate at which substantial reaction has occurred. Due to a low growth temperature, the film is quite defective and in addition shows the extra CuO planes characteristic of the "247" and "248" phases as darker lines separating pairs of bright Ba columns. We can see directly how the bright Ta columns of the substrate fade into the positions of the Cu columns (unresolved) in the superconductor and how the K of the substrate (again not visible) turns into the Ba columns in the superconductor. For one or two unit cells, we even see the Ta and Ba columns simultaneously indicating

the presence of an appreciable transition zone at the interface.

6. CONCLUSIONS

Direct imaging of structure and composition can be achieved at atomic resolution using the Howie detector in a STEM. The intuitive interpretability arises from the suppression of dynamical effects so that contrast arises primarily from changes in column composition. This occurs in the following manner:

1. The coherent STEM probe causes Bloch states in the crystal to be integrated over a significant angular range. Tightly bound, nondispersive s-type states add constructively, whereas less localized states interfere destructively.
2. The Howie detector senses the incoherently generated intensity very close to the atomic sites, further enhancing the importance of s-type states over the less localized states.
3. In perfect crystals, the thickness integration reduces dynamical oscillations to second order, with the result that contrast is dominated by the almost Z^2 dependence of the scattering cross sections.
4. The s-states are highly localized and contribute to the image via their integrated intensity, not their emergent phase. Their contribution to the image is, therefore, generally unaffected by their surroundings so that intuitive interpretation holds for planar defects, interfaces or superlattices.
5. With increasing thickness, the contrast reduces as the s-state becomes depleted, but the resolution is preserved. Resolution is controlled by the probe intensity profile at the entrance surface of the crystal.

The most important benefit of a direct image is the fact that the image itself provides the first order most likely model structure; unanticipated interface structures will be immediately apparent. This structure can then be accurately simulated through calculations of axial Bloch states and the dispersion surface and refined in the usual way by comparison with experiment. This capability offers a new level of insight into the atomistic processes of growth and the origin of interfacial properties.

Acknowledgements—We are grateful to J.-M. Baribeau, R. Feenstra, D. P. Norton and D. H. Lowndes for provision of samples, and S. L. Carney, J. T. Luck and T. C. Estes for technical assistance. This research was sponsored by the Division of Materials Sciences, U.S. Department of Energy, under contract DE-AC05-84OR21400 with Martin Marietta Energy Systems, Inc.

REFERENCES

1. S. J. Pennycook and D. E. Jesson, *Phys. Rev. Lett.* **64**, 938 (1990).
2. S. J. Pennycook and D. E. Jesson, *Ultramicrosc.* **37**, 14 (1991).
3. A. Howie, *J. Microsc.* **117**, 11 (1979).
4. M. M. J. Treacy and S. B. Rice, *J. Microsc.* **156**, 211 (1989).
5. A. Engel, J. W. Wiggins and D. C. Woodruff, *J. appl. Phys.* **45**, 2739 (1974).
6. M. S. Isaacson, M. Ohtusuki and M. Utlaut, in *Introduction to Analytical Electron Microscopy* (edited by J. J. Hren, J. I. Goldstein and D. C. Joy), p. 343. Plenum Press, New York (1979).
7. D. E. Jesson, S. J. Pennycook and M. F. Chisholm, in *Atomic Scale Structure of Interfaces* (edited by R. D. Brigans, R. M. Feenstra and J. M. Gibson), p. 439. Materials Research Society, Pittsburgh, Pa (1990).
8. D. E. Jesson and S. J. Pennycook *Proc. R. Soc.*, submitted.
9. C. R. Hall, *Phil. Mag.* **12**, 815 (1965).
10. D. M. Bird and A. G. Wright, *Acta crystallogr. A* **45**, 104 (1989).
11. C. R. Hall and P. B. Hirsch, *Proc. R. Soc. A* **286**, 158 (1965).
12. D. Cherns, A. Howie and M. H. Jacobs, *Z. Naturf.* **28a**, 565 (1973).
13. S. J. Pennycook and A. Howie, *Phil. Mag.* **41**, 809 (1980).
14. Z. L. Wang and J. M. Cowley, *Ultramicrosc.* **31**, 437 (1989).
15. Z. L. Wang and J. M. Cowley, *Ultramicrosc.* **32**, 275 (1990).
16. S. Takagi, *J. Phys. Soc. Japan* **13**, 278 (1958).
17. Z. L. Wang and J. Bentley, *Ultramicrosc.* **37**, 39 (1991).
18. P. A. Doyle and P. S. Turner, *Acta crystallogr. A* **24**, 390 (1968).
19. S. J. Pennycook, S. D. Berger and R. J. Culbertson, *J. Microsc.* **144**, 229 (1986).
20. H. Fleischmann, *Z. Naturf.* **15a**, 1090 (1960).
21. F. Salvat, *Phys. Rev. A* **43**, 578 (1991).
22. D. D. Perovic, G. C. Weatherly, R. F. Egerton, D. C. Houghton and T. E. Jackman, *Phil. Mag. A* **63**, 757 (1991).
23. J. Fertig and H. Rose, *Optik* **59**, 407 (1981).
24. R. J. Loane, E. J. Kirkland and J. Silcox, *Acta crystallogr. A* **44**, 912 (1988).
25. K. Kambe, *Ultramicrosc.* **10**, 223 (1982).
26. D. Van Dyck, J. Danckaert, W. Coene, E. Selderslaughs, D. Broddin, J. Van Landuyt and S. Amelinckx, in *Computer Simulation of Electron Microscopy Diffraction and Images* (edited by W. Krakow and M. O'Keefe), pp. 107–134. TMS (1989).
27. K. Kambe, G. Lehmpfuhl and F. Fujimoto, *Z. Naturf.* **29a**, 1034 (1974).
28. B. F. Buxton, J. E. Loveluck and J. W. Steeds, *Phil. Mag. A* **38**, 259 (1978).
29. D. E. Jesson, S. J. Pennycook and J.-M. Baribeau, in *High Resolution Electron Microscopy of Defects in Materials* (edited by R. Sinclair, D. J. Smith and U. Dahmen), pp. 230–233. Materials Research Society, Pittsburgh, Pa (1990).
30. D. M. Bird and Q. A. King, *Acta crystallogr. A* **46**, 202 (1990).
31. F. Beech, S. Miragalia, A. Santoro and R. S. Roth, *Phys. Rev. B* **35**, 8778 (1987).
32. D. H. Shin, E. J. Kirkland and J. Silcox, *Appl. Phys. Lett.* **55**, 2456 (1989).
33. P. Xu, E. J. Kirkland, J. Silcox and R. Keyse, *Ultramicrosc.* **32**, 93 (1990).
34. O. Scherzer, *J. appl. Phys.* **20**, 20 (1949).
35. S. J. Pennycook, D. E. Jesson and M. F. Chisholm, in *Nanostructures and Microstructure Correlation with Physical Properties of Semiconductors* (edited by H. G. Craighead and J. M. Gibson), pp. 182–194. SPIE, Bellingham (1990).
36. S. J. Pennycook, D. E. Jesson and M. F. Chisholm, in *Proc. 7th Oxford Conf. on Microscopy of Semiconducting Materials* (edited by A. G. Cullis and N. J. Long), pp. 27–35. Institute of Physics, London (1991).
37. D. E. Jesson, S. J. Pennycook and J.-M. Baribeau, *Phys. Rev. Lett.* **66**, 750 (1991).
38. S. J. Pennycook, M. F. Chisholm, D. E. Jesson, D. P. Norton, D. H. Lowndes, R. Feenstra, H. R. Kerchner and J. O. Thomson, *Phys. Rev. Lett.* **67**, 765 (1991).